Plasma Sources Science and Technology

PAPER • **OPEN ACCESS**

Pulse length dependence of a reactive high power impulse magnetron (HiPIMS) discharge

To cite this article: R Hippler *et al* 2023 *Plasma Sources Sci. Technol.* **32** 055013

OPEN ACCESS
IOP Publishing
Plasma Sources Science and Technology
Plasma Sources Sci. Technol. **32** (2023) 055013 (12pp)
https://doi.org/10.1088/1361-6595/acd5fc

Pulse length dependence of a reactive high power impulse magnetron (HiPIMS) discharge

R Hippler[1,2,*], M Cada[1], A Mutzke[3] and Z Hubicka[1]

[1] Institute of Physics, Czech Academy of Sciences, Na Slovance 2, 18221 Prague, Czech Republic
[2] Institut für Physik, Universität Greifswald, Felix-Hausdorff-Str. 6, 17489 Greifswald, Germany
[3] Max-Planck-Institut für Plasmaphysik, Wendelsteinstraße 1, 17491 Greifswald, Germany

E-mail: hippler@physik.uni-greifswald.de

Received 16 January 2023, revised 24 April 2023
Accepted for publication 16 May 2023
Published 2 June 2023

Abstract

The pulse length dependence of a reactive high power impulse magnetron sputtering (HiPIMS) discharge with a tungsten cathode in an argon+oxygen gas mixture gas was investigated. The HiPIMS discharge is operated with a variable pulse length of 20–500 μs. Discharge current measurements, optical emission spectroscopy of neutral Ar, O, and W lines, and energy-resolved ion mass spectrometry are employed. A pronounced dependence of the discharge current on pulse length is noted while the initial discharge voltage is maintained constant. Energy-resolved mass spectrometry shows that the oxygen-to-tungsten (O^+/W^+) and the tungsten oxide-to-tungsten (WO^+/W^+) ion ratio decreases with pulse length due to target cleaning. Simulation results employing the SDTrimSP program show the formation of a non-stoichiometric sub-surface compound layer of oxygen which depends on the impinging ion composition and thus on the pulse length.

Keywords: high power impulse magnetron sputtering, reactive mode, pulse length dependence, ion composition, optical emission spectroscopy

(Some figures may appear in colour only in the online journal)

1. Introduction

Magnetron sputtering (MS) is a physical vapour deposition method [1]. Due to its simplicity, MS has become widely used for deposition of metallic and compound thin solid films [2]. A typical MS discharge consists of a negatively biased cathode which is operated in the glow discharge regime. A magnetic field supplied by permanent magnets underneath the cathode is employed to enhance the plasma (electron, ion) density in front of the cathode. The combination of magnetic and electric fields creates a magnetic trap confining electrons to a region above the cathode. This electron trap constitutes a region of high ionisation probability where electrons undergo ionising collisions with gas atoms. Positively charged ions are attracted by the negatively biased cathode. The resulting ion bombardment causes emission of secondary electrons which are repelled by the cathode and help to sustain the discharge. In addition, bombarding ions are implanted into the cathode's surface and cause the erosion of the cathode through sputtering of atoms.

MS discharges are frequently operated with argon as working gas for deposition of thin metallic films. Reactive MS has been invented for deposition of compound (e.g. oxide or nitride) thin films. The addition of a reactive gas, e.g. oxygen or nitrogen, to the discharge introduces several additional complications. Most notable are (i) the partial or total covering of the cathode's surface by the reactive gas followed

* Author to whom any correspondence should be addressed.

by physical and/or chemical surface processes leading to the formation of an ultrathin, e.g. oxide or nitride layer and (ii) the formation of a sub-surface compound layer through implantation of plasma ions [3]. Surface modifications change the electronic structure of the surface which influences secondary electron emission and sputtering yield [4]. The sputtering yield of a compound is often reduced compared to a metallic surface and so is the deposition rate which shows a non-linear dependence on the reactive gas flow rate [2].

Magnetron discharges are operated in various regimes and with different, e.g. direct current, radiofrequency, and pulsed modes. In recent years, so-called high power impulse magnetron sputtering (HiPIMS) has received much attention due to its particular suitability for thin film deposition [2, 5–8]. HiPIMS utilises short pulses and low repetition rates and offers large plasma densities and larger ion energies compared to direct current MS (DCMS) [5–11]. Due to the pulsed operation, HiPIMS discharges are operated under non-stationary plasma conditions. This has certain consequences regarding the interaction with reactive gas species. The second process (ii) is essentially limited to the pulse *on* regime. On the other hand, process (i) is not limited to the pulse *on* time but continues during the pulse *off* phase. It implies that the surface coverage with the reactive gas will decrease during the pulse *on* time and increase again during the pulse *off* phase and eventually may reach the maximum possible surface coverage prior to the next pulse.

In this context, the surface coverage θ (see equation (1) below) is defined as the fraction of occupied docking sites by adsorbing atoms. The number of docking sites at the surface is determined by the area density of surface atoms which may depends on the crystal structure. The maximum (full) surface coverage $\theta_0 = 1$ is reached once all docking sites are occupied. As an example, for O atoms on a W(100) surface, the maximum surface coverage θ_0 is reached when the oxygen-to-tungsten (O/W) ratio on the top surface equals 1 [12] which is much smaller than the stoichiometry ratio of a WO_3 crystal.

There is an ongoing challenge to further enhance the energy-influx during film deposition making use of so-called bipolar pulsing, a positively biased anode, and the use of an external anode [13–15]. Another approach is to vary the employed pulse length which influences ion composition and ion energy during the discharge and thus affects the deposition rate, the composition, and other properties of deposited thin films [16–28]. An alternative approach was employed by Magnus *et al* [29] varying the pulse frequency and, hence, the time between two subsequent pulses. A thorough understanding of the involved mechanisms during reactive HiPIMS and of the corresponding time dependence is yet lacking, however. In the present paper we examine the variation of discharge properties as function of pulse length of a reactive HiPIMS discharge with a tungsten target in an $Ar+O_2$ gas mixture. Discharge current, energy-resolved mass spectrometry, and time-resolved optical emission spectroscopy (OES) of selected Ar, O, and W lines are investigated as function of pulse length in the range 20–500 μs. Results are compared with theoretical estimates for the oxygen surface coverage and the formation of a sub-surface compound layer at the cathode.

2. Experiment

The experimental set-up used in this study has been described before [30–32]. A planar magnetron equipped with a W target (diameter 50.8 mm, nominal thickness 6 mm, purity 99.95%) is employed. The discharge is operated in an $Ar+O_2$ gas mixture using two gas flow controllers with equal gas flow rates of 10 sccm for Ar and 10 sccm for O_2. The pressure is measured with a capacitance vacuum gauge. The nominal gas pressure is set to $p = 1.0$ Pa. The magnetron sputtering discharge is powered by a DC power supply (Advanced Energy MDX–1 K) which is operated in constant voltage mode. Pulsed operation is achieved in combination with a home-built power switch delivering a negative pulse during the discharge [33–36]. Repetition frequency and pulse length are both controlled with the help of an arbitrary waveform generator (OWON AG 1022). Measurements are carried out by varying the pulse length between 20 μs and 500 μs with the same repetition rate of 100 Hz. In this way, the time between subsequent pulses is kept constant which is important to achieve the same surface coverage prior to each pulse. Voltage and current waveforms are simultaneously recorded using voltage (Agilent 10076 A) and current probes (Textronix A622) connected to a two-channel digital oscilloscope (Agilent DSO 6012A). The floating potential (FP) is measured with an electrical probe hanging down from the top flange. The probe tip is placed 5 cm from the cathode in axial direction. The FP is recorded with the same voltage probe and oscilloscope as described above [15].

The discharge voltage measured at the cathode and the measured FP as a function of time for a 100 μs pulse length are displayed in figure 1. The discharge voltage initially drops to -878 V, temporarily increases to -863 V within the next 5 μs, and slowly decreases to -878 V towards the pulse's ending. The simultaneously measured FP reaches a minimum of -1.8 V after 8 μs; it becomes positive after 14 μs and increases further to $+3.5$ V after 60 μs. It approximately remains at this level until the end of the pulse. The FP shows a rapid decay after the pulse's ending followed by an approximately exponential decay during the afterglow with an estimated decay time of about 3.3 ms.

The mean discharge power as shown in figure 2 was obtained by numerical integration of the measured current and voltage characteristics; the calculated values agree well with the discharge power shown by the power supply. The discharge power for a constant initial discharge voltage of -810 V increases monotonously as a function of pulse length; the increase can be linked to an increasing duty cycle. Also shown in figure 2 is the gas pressure which decreases with increasing pulse length indicating a significant gas (oxygen) consumption with increasing discharge power.

The discharge power as function of oxygen gas flow rate is shown in figure 3. During the measurements, the initial discharge voltage was maintained at -810 V. The discharge power drops from 300 W without oxygen to about 27 W at an O_2 gas flow rate of 1 sccm; it increases to about 43 W when the O_2 gas flow rate is raised to 10 sccm. Similar dependencies, though less pronounced, have been observed before and

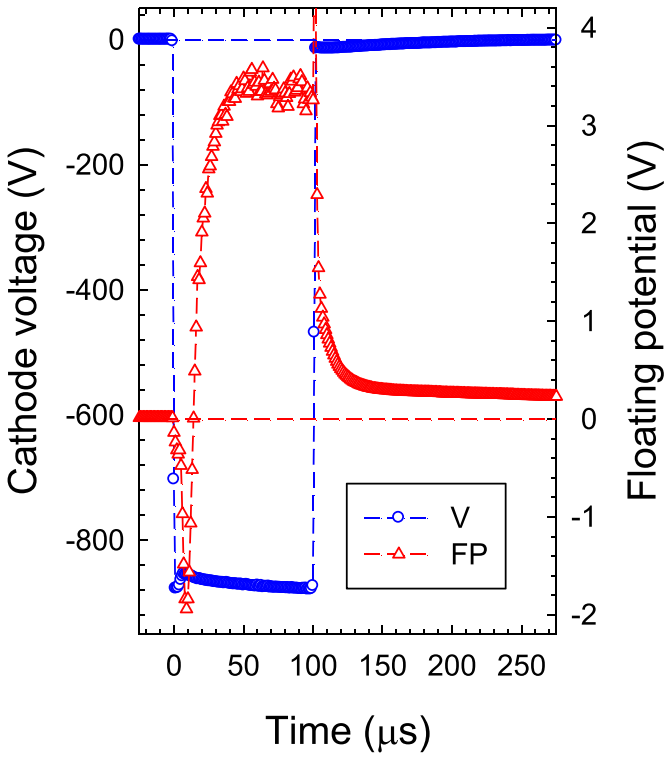

Figure 1. Discharge voltage (V) and floating potential (FP) *versus* time. The HiPIMS discharge was operated with an initial voltage of −900 V. Argon flow rate 10 sccm, O_2 flow rate 10 sccm, gas pressure 1.0 Pa.

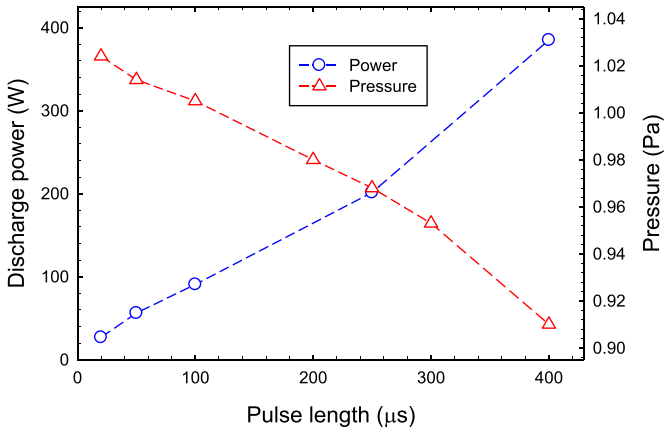

Figure 2. Mean discharge power and gas pressure *versus* pulse length. The HiPIMS discharge was operated with an initial voltage of −970 V and with a constant repetition frequency of 100 Hz. Argon gas flow rate 10 sccm, O_2 gas flow rate 10 sccm.

attributed to the formation of a (partial) surface coverage of the cathode with oxygen [37, 38].

The optical emission from the plasma is recorded with a Shamrock SR500D spectrometer (focal length 500 mm) equipped with an iCCD detector (iStar DH334T, Andor Technology, Belfast, Northern Ireland). The spectrometer is equipped with three gratings. The reported measurements are carried out employing a grating with 600 lines per millimetre which offers the largest spectral range of the three gratings

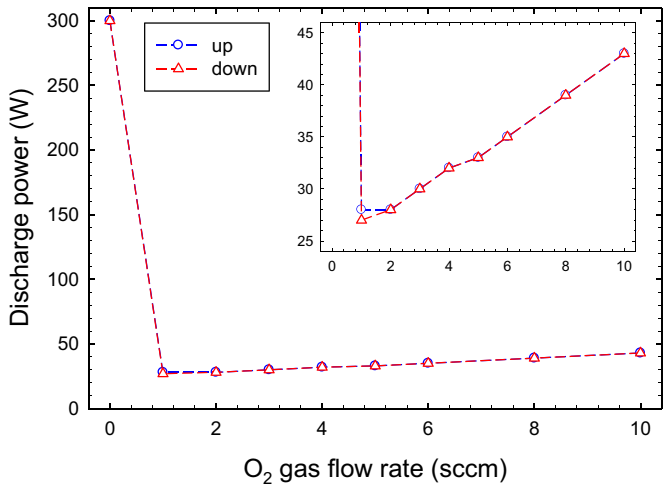

Figure 3. Mean discharge power *versus* O_2 gas flow rate. The HiPIMS discharge was operated with an initial voltage of −810 V and with a pulse length of 100 μs. Argon gas flow rate 10 sccm. Inset shows expanded view.

albeit with a smaller but still more than sufficient spectral resolution of about 0.5 nm. The spectrograph is equipped with a filter wheel in front of the entrance slit to suppress second order lines. An optical fibre connected to the entrance slit (slit width 10 μm) of the spectrometer is installed outside the vacuum chamber at an angle of 45° with respect to the target surface normal. Time-resolved OES measurements are performed with a gate width of 10 μs and with incremental gate steps of 10 μs. Optical emission spectra recorded during the time-resolved measurements are displayed in figure 4. The *violet* spectrum is recorded at wavelengths of 398–442 nm. It displays several strong neutral tungsten (W) and ionised Ar^+ lines. No lines from neutral Ar are detected in this range. As noted before, Ar I lines in this wavelength range are presumably quenched due to de-excitation to other excited Ar states [38]. The *near-infrared* spectrum recorded at wavelengths of 742–782 nm is chosen as it displays the strong Ar I emission lines with wavelengths in the 750–772 nm range and the O I triplet at 777.19/777.42/777.54 nm.

Ion energy distributions are measured with the help of energy-resolved mass spectrometry [31, 32]. Tungsten has five natural isotopes with mass numbers m in the range $m = 180$–186 (table 1). Most abundant is the W–184 isotope which is employed during the present investigation. A typical ion mass spectrum obtained with a HiPIMS discharge in an Ar+O_2 gas mixture is shown in figure 5. Most abundant are atomic O^+ ($m/z = 16$), O_2^+ ($m/z = 32$), and Ar^+ ($m/z = 40$) ions, where z is the charge number. Singly charged W^+ and doubly charged W^{2+} ions from the tungsten cathode appear in the range $m/z = 182$–186 and $m/z = 91$–93, respectively. A large fraction of tungsten is oxidised. The corresponding WO^+, WO_2^+, and WO_3^+ ions are observed at mass numbers in the range $m/z = 198$–202, $m/z = 214$–218, and $m/z = 230$–234, respectively. In addition, ArO^+ and doubly charged WO^{++} ions at mass numbers $m/z = 56$ and $m/z = 99$–101, respectively, are observed.

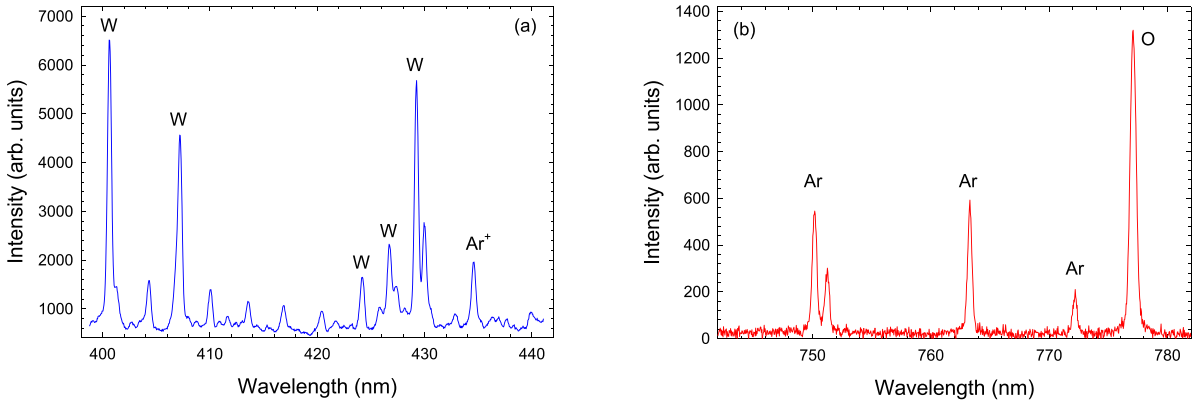

Figure 4. Time-averaged optical emission spectrum in the (a) violet ($\lambda = 398$–442 nm) and (b) near-infrared ($\lambda = 742$–782 nm) wavelength regime. Initial discharge voltage -950 V. Pulse width 100 μs.

Table 1. Relative abundance of tungsten isotopes [39].

Isotope	180	182	183	184	186
Abundance (%)	0.12	26.50	14.31	30.64	28.43

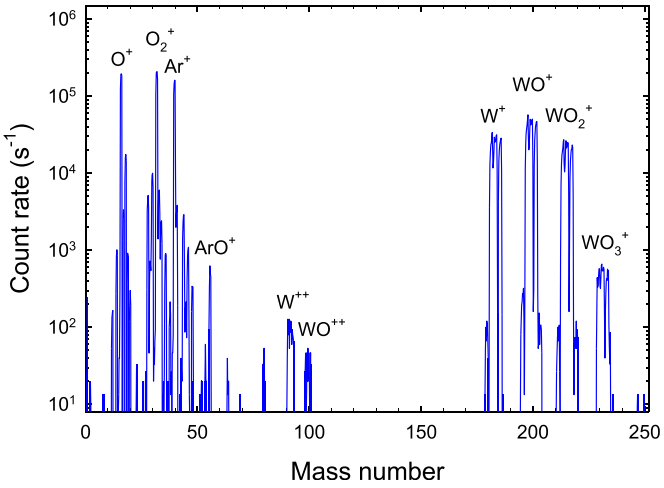

Figure 5. Ion mass spectrum for a HiPIMS discharge. Ar flow rate 10 sccm, O_2 flow rate 10 sccm, gas pressure 1.75 Pa, discharge power 60 W, pulse length 100 μs.

3. Simulation

Yield and target composition calculations are performed with the Monte Carlo program SDTrimSP [40]. The program is based on the binary-collision approximation (BCA) [41] and assumes an amorphous (randomised) target structure at room temperature and an infinite lateral size [42]. It can be run in static or dynamic mode on sequential or parallel systems. In the static mode, the composition of the target is predefined and kept fixed during the simulation, while in the dynamic mode the compositional changes of the target material are calculated self-consistently. Examples of modelings and comparison with measurements of a tungsten target are shown in [42]. Bombardment with noble gas projectiles are in good agreement with experimental data [43].

The implantation of atoms in the target changes the density and the composition inside the solid and has, therefore, an influence on the depth profile and on sputtering. Due to the low binding energy of gas atoms (nearly zero for noble gases) they get more easily sputtered. Another effect of the low binding energy is the possible out-gasing of gas atoms. The implanted and not bounded gas atoms in the target cannot move independently. Only the presence of defects during the bombardment causes a local diffusion [40].

4. Results

4.1. Current waveforms

The temporal evolution of measured current waveforms for different initial discharge voltages (-600 V to -950 V) and for pulse lengths of 25 μs, 50 μs, 100 μs, 300 μs, and 500 μs are displayed in figure 6. The discharge current during, e.g. the 50 μs pulse shows an ignition delay varying between 21 μs and 6 μs for initial discharge voltages of -600 V and -950 V, respectively. After the ignition, the discharge current increases, reaching a maximum after 20–25 μs followed by a gradual decrease during longer pulses which is attributed to gas rarefaction [44, 45]. The discharge current maximum (below 100 μs) strongly increases as function of the applied discharge voltage (figure 6(f)). We want to emphasise that the discharge current is significantly higher for short pulses compared to long pulses during the first 25 μs. It indicates that the evolution of a new pulse is influenced by the previous pulse. The discharge current rises again after 100 μs as is evident for the 300 μs and 500 μs pulses. A current increase for long pulses was observed by Aiempanakit *et al* for operation in so-called oxide mode [46]. In this time regime, the current waveform approaches the triangular shape typical for reactive HiPIMS [47, 48]. It is believed that the main reason for this behaviour is due to the cathode's surface covered by adsorbed and implanted oxygen atoms and a changing surface composition during the pulse. The observation is in agreement with results of Kubart and Aijaz [49, 50] who attribute the enhanced discharge current to a different surface stoichiometry of oxygen.

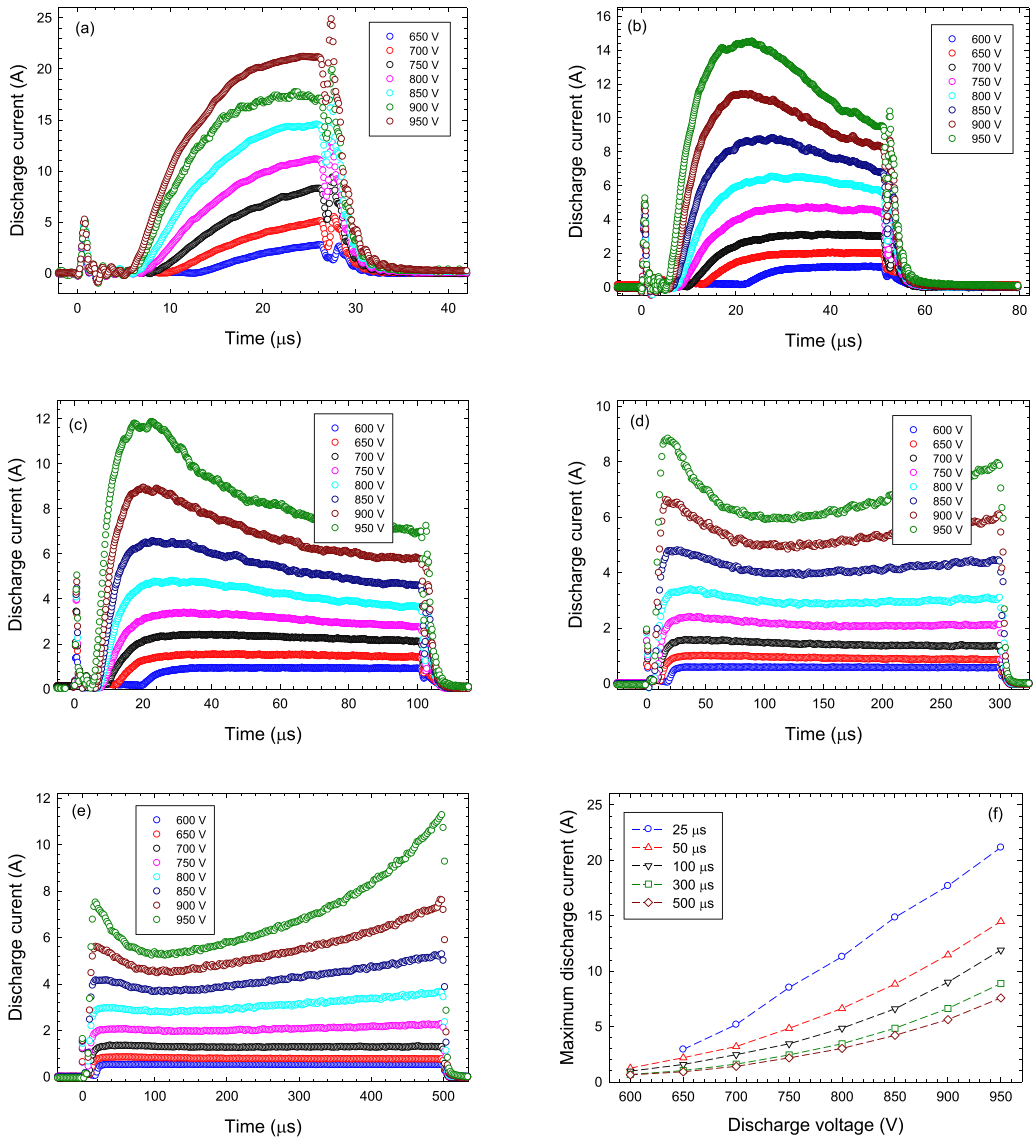

Figure 6. Discharge current *versus* time for pulse lengths of (a) 25 μs, (b) 50 μs, (c) 100 μs, (d) 300 μs, and (e) 500 μs of a HiPIMS discharge and for initial discharge voltages of 600–950 V, (f) maximum discharge current (during the first rise up to 100 μs) *vs.* initial discharge voltage for different pulse width of 25–500 μs. Ar gas flow rate 10 sccm, O_2 gas flow rate 10 sccm, gas pressure 1.0 Pa.

4.2. Optical emission spectroscopy

The time evolution of Ar I, W I, O I, and Ar II optical emission lines and of the oxygen-to-tungsten (O/W) ratio for different pulse lengths in the range 50–500 μs are displayed in figure 7. In order to maintain the same discharge conditions, the initial discharge voltage was kept at a constant value. The intensity of the Ar I emission line rapidly increases during the first 15 μs right after ignition followed by a fast decrease to a medium intensity level during the next 30 μs and, for the longer pulses, a slow decreases towards the pulse's ending. Where comparable, the temporal behaviour is rather similar and independent of the pulse length. The intensity of the W I line behaves differently. Again, there is a rapid although somewhat slower increase during the first 25 μs right after ignition but the maximum intensity reached during the first 50 μs of the pulse differs significantly as function of pulse length with the shortest pulses achieving the largest intensity. A renewed increase in intensity is noted for longer pulse lengths of 300 μs and 500 μs. The W I intensity, hence, is reminiscent of the behaviour of the discharge current, in particular, a larger intensity/current for short pulses, a falling intensity between 25 μs and 100 μs, and a renewed increase of current/intensity after 100 μs for longer pulses. Propagation of sputtered metal atoms as observed for Ti atoms may also contribute to the observed intensity increase after 100 μs [25, 51].

Similar time dependencies were reported by Shimizu *et al* [52] for a HiPIMS discharge with a tungsten target in pure argon. Accordingly, for a pulse length of 100 μs, the Ar I emission line reaches its intensity maximum within about 10 μs which is followed by a gradual decline. The intensity of other (Ar II, W I, and W II) emission lines show a less pronounced intensity increase reaching the maximum intensity after about 35 μs [52].

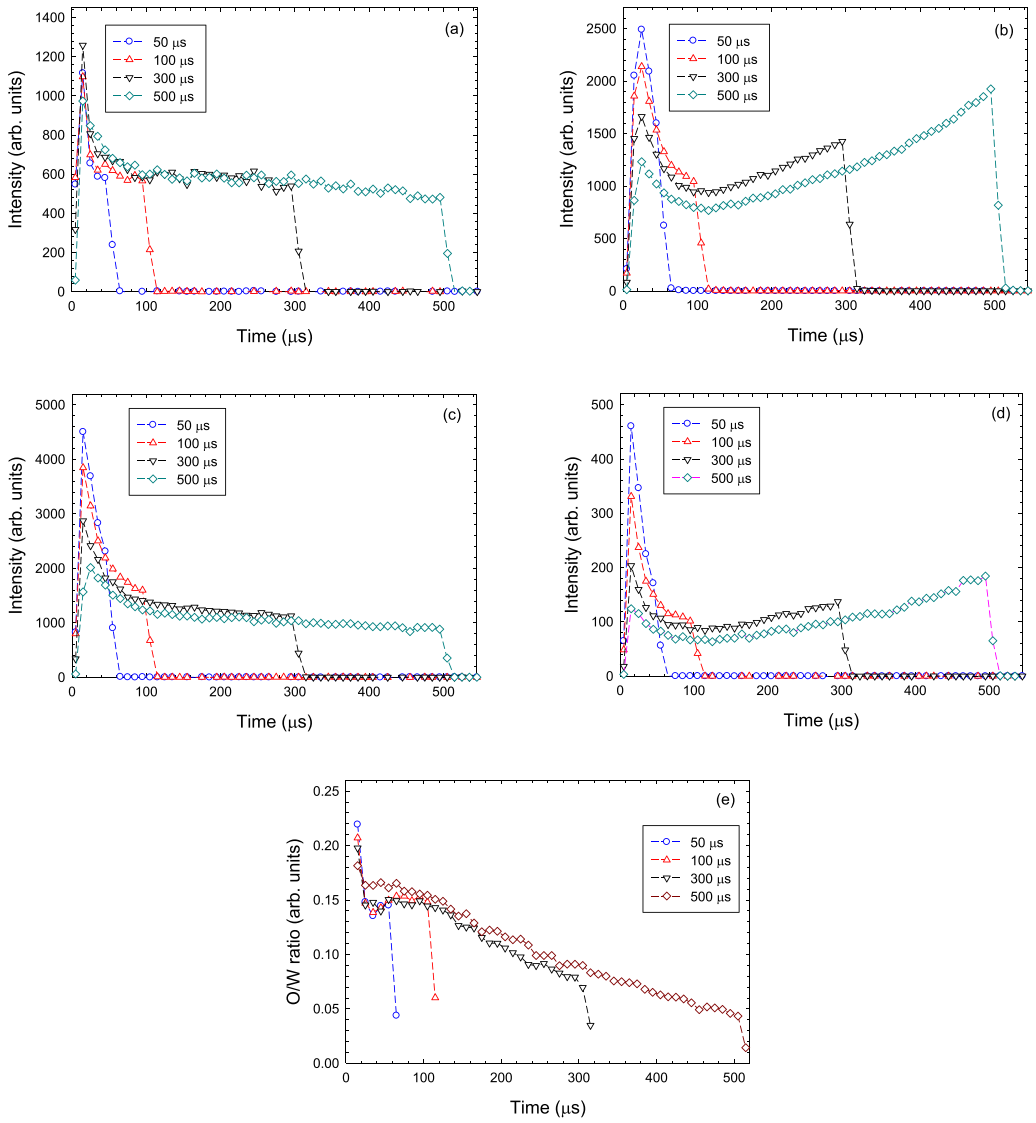

Figure 7. Temporal evolution of (a) Ar I (763 nm), (b) W I (429 nm), (c) O I (777 nm), (d) Ar II (434 nm) emission lines and of the (e) oxygen-to-tungsten (O/W) ratio for different pulse lengths in the range of 50–500 μs. Initial discharge voltage −950 V. Ar gas flow rate 10 sccm, O_2 gas flow rate 10 sccm, gas pressure 1.0 Pa.

The intensity of the O I line also displays a large intensity difference during the first 50 μs for different pulse length. Unlike the W I line, a rising intensity for longer pulses is not observed, however. The largest intensity variation is observed for the Ar II emission line. The line is emitted by excited Ar^{+*} ions which are produced either by direct excitation of Ar^+ ions or via simultaneous excitation and ionisation of neutral Ar atoms. The second process requires a rather large energy transfer and is believed to arise from collisions of energetic secondary electrons ejected from the cathode [38]. The existence of such energetic electrons has been reported before [53, 54].

The O/W ratio deduced from the OES measurements displays a rapid decline within the first 25 μs which is followed by a more gradual decrease towards the end of the pulse. The different behaviour of, in particular, W I and O I emission lines indicates that the cathode's surface coverage with oxygen decreases during longer pulses yielding to an enhanced sputtering rate for tungsten atoms.

4.3. Energy-resolved mass spectrometry

In order to elucidate this point further, we investigate the ion energy distributions of plasma ions obtained by energy-resolved mass spectrometry which are displayed in figure 8. Measurements are shown for W^+, WO^+, WO_2^+, O^+, and Ar^+ ions. O^+, O_2^+ (not shown), and Ar^+ are the most abundant ions. Tungsten and tungsten oxide ions are produced via sputtering from the tungsten cathode and the subsequent ionisation in the plasma region close to cathode. The initial energy distribution near the cathode follows from sputtering theory and is characterised by a pronounced high-energy component [32, 55]. We mention in passing that the energy distribution predicted by sputtering theory holds for sputtering of monoatomic atoms and ions (e.g. W^+) while for polyatomic atoms and ions (e.g. WO^+ and WO_2^+) a steeper energy dependence is observed [56, 57]. The present results are in qualitative agreement with previous observations. There are at least two

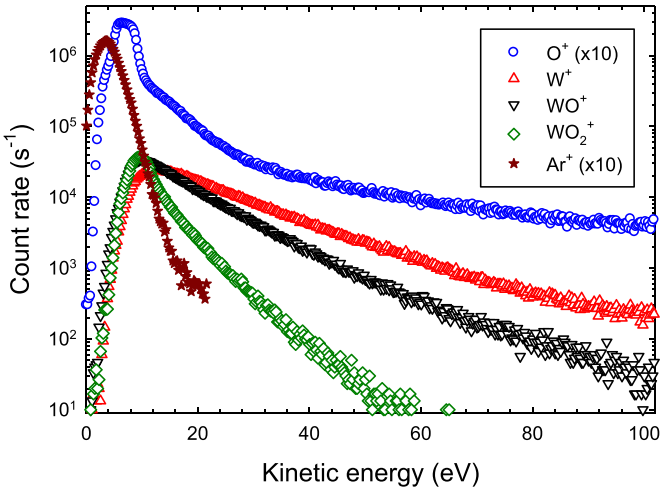

Figure 8. Energy distribution of W^+ ($m/z = 184$, ○), WO^+ ($m/z = 200$, △), WO_2^+ ($m/z = 216$, ▽), O^+ ($m/z = 16$, ◇), and Ar^+ ($m/z = 40$, ⋆) ions for a HiPIMS discharge with a pulse length of 250 μs. Initial discharge voltage −970 V. Ar gas flow rate 10 sccm, O_2 gas flow rate 10 sccm, gas pressure 1.0 Pa.

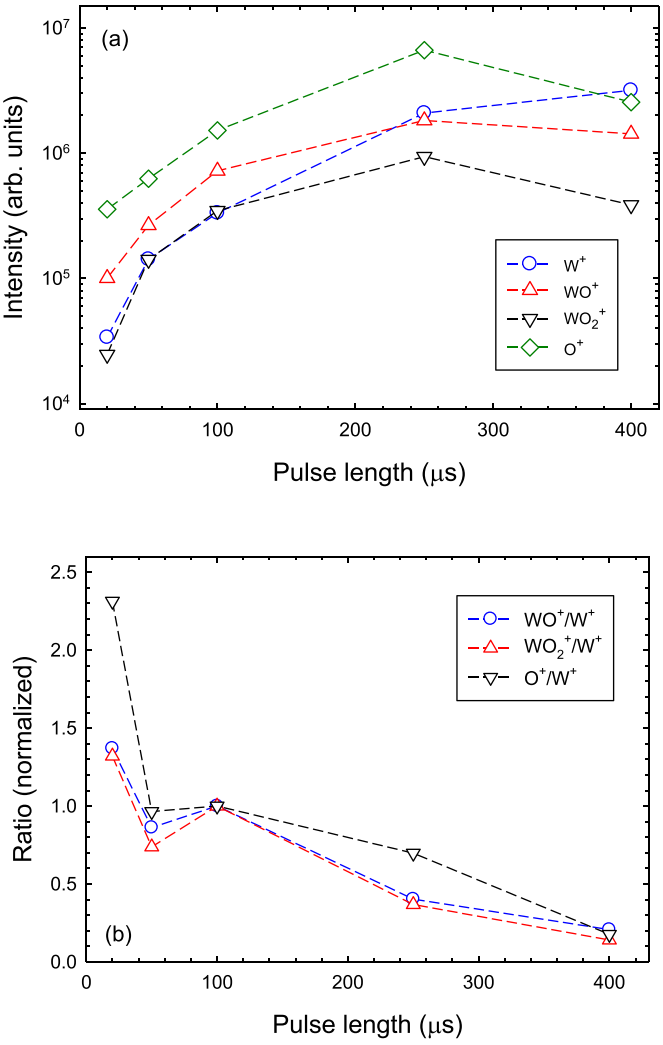

Figure 9. (a) Energy-integrated ion intensity of W^+ ($m/z = 184$), WO^+ ($m/z = 200$), WO_2^+ ($m/z = 216$), and O^+ ($m/z = 16$) ions and (b) the normalised WO^+/W^+, WO_2^+/W^+, and O^+/W^+ ratios *versus* pulse length for a HiPIMS discharge with pulse lengths of 20–400 μs. Initial discharge voltage −970 V. Ar gas flow rate 10 sccm, O_2 gas flow rate 10 sccm, gas pressure 1.0 Pa.

different mechanisms for O^+ ion production, i.e. sputtering from the oxidised cathode and O^+ formation via ionisation of slow oxygen atoms or dissociative ionisation of O_2 molecules in the gas phase. The first process gives rise to the production of energetic ions with large kinetic energies while O^+ ions which form in gas phase should have small kinetic energies of typically less than 20 eV. The measured energy distribution of O^+ ions is indeed characterised by a pronounced high-energy tail above about 20 eV which we attribute to sputtering of oxygen atoms from the cathode (figure 8). For comparison, we also display our results for Ar^+ ions which are characterised by a pronounced low-energy contribution produced in gas phase collisions but do not show any high-energy tail.

The energy-integrated ion intensity of W^+ ions increases with pulse length (figure 9(a)). In part, the increase is due to an increase of the duty cycle. Intensities of WO^+, WO_2^+, and O^+ ions at first also increase with pulse length. The increase is less pronounced, however, and intensities even decrease for the largest pulse length of 400 μs. Figure 9(b) shows the WO^+/W^+, WO_2^+/W^+, and O^+/W^+ intensity ratios. From 20 μs to 400 μs, the WO^+/W^+ and WO_2^+/W^+ ratios decrease by factors of more than 6 and 9, respectively, (figure 9). The O^+/W^+ ratio even decreases by a factor of 13. The result is in line with the OES measurements as the O I emission monotonously decreases with time while the W I intensity after an initial decline increases again (figure 7). The results indicate that with increasing pulse length less oxygen is available at the cathode due to a lower surface coverage and, as a consequence, the intensity of oxygen and oxygen-containing ions decreases.

5. Discussion

It is known that the covering of a metal surface with oxygen influences sputtering as well as secondary electron and light emission processes processes [4, 58–61]. The here observed pronounced decrease of the discharge power (figure 3) is explained by a strong reduction of the secondary electron emission yield (SEEY) due to the cathode's oxygen coverage [4]. Three stages as function of oxygen coverage have been identified in a recent investigation [61]. Already at low oxygen (sub-monolayer) coverage, the formation of a surface potential barrier hinders secondary electron emission [61]. Further increasing the oxygen coverage, however, reduces the surface barrier and the SEEY increases again. In the third phase the surface is fully covered and an oxide layer forms. The workfunction of tungsten oxide is larger compared to clean tungsten, however, remains smaller compared to a partially oxidised (sub-stoichiometric) surface. The SEEY of a fully oxidised surface is, hence, larger compared to a partially oxidised surface but remains smaller compared to a clean tungsten surface [62]. The model, hence, can explain the power decrease for low and the power increase for larger oxygen gas flows. We would like to emphasise that the model presented by

Li *et al* [61] is not fully compatible with our situation as the cathode's material (W *vs.* Al) and the employed ion energies are widely different.

In order to explain the observed pulse length dependencies (figures 6 and 7), we consider the time-dependent tungsten surface coverage with oxygen during the pulse *on* and *off* time. Starting with a single oxygen layer on the tungsten surface which builds up during the pulse *off* time, the surface coverage decreases during the pulse *on* time by the interaction with plasma ions and the subsequent sputtering of oxygen atoms. The time evolution of the surface coverage can be expressed by a rate equation [60]

$$\frac{\mathrm{d}\theta}{\mathrm{d}t} = -\frac{\Phi_+ Y_\mathrm{O}}{N_s}\,\theta + \frac{\Phi_\mathrm{O} c_s}{N_s} \times (1-\theta) \qquad (1)$$

where $\theta = \theta(t)$ is the time-dependent surface coverage, Φ_+ is the ion flux density, Y_O is the sputtering (desorption) yield of O atoms, Φ_O is the oxygen flux to the surface, c_s is the sticking coefficient of oxygen, and N_s is the saturation surface density of oxygen. The saturation surface density (beyond which no sticking occurs) depends on the crystal orientation of the tungsten surface. The sticking coefficient c_s depends on the surface coverage and on the surface orientation. The initial sticking coefficient is 0.5 for a clean W(100) and 1.0 for a clean W(110) surface [12]. The sticking coefficient decreases monotonously with increasing surface coverage. For simplicity, a constant (averaged) sticking coefficient $c_s = 0.4$ and a surface density $N_s = 1.4 \times 10^{19}\,\mathrm{m}^{-2}$ are here employed. According to Wang and Gomer [12], the maximum oxygen coverage of a W(100) surface corresponds to an oxygen-to-tungsten (O/W) ratio of 1 which is much smaller than the O/W ratio expected for a fully oxidised WO_3 solid. The sputtering (desorption) yield $Y_\mathrm{O} \approx 1.4$ of oxygen is evaluated from the work of Taglauer *et al* assuming Ar^+ ion bombardment with a kinetic energy of 1 keV [59]. Cross sections $\sigma_d = 3.9 \times 10^{-19}\,\mathrm{m}^2$ for desorption of oxygen atoms from a Ni surface by Ar^+ impact were measured at an incidence angle $\psi = 30^\mathrm{o}$ with respect to the surface. Corresponding desorption cross sections for oxygen on a W surface are ≈17% smaller. For normal incidence, we have to apply a correction $\cos^{-f}\phi$, where $\phi = 1 - \psi$ is the incidence angle with respect to the surface normal and $f \approx 1.67$ [63], in reasonable agreement with experimental results [64, 65].

The surface coverage θ obtained with the help of equation (1) is shown in figure 10, where $\theta = 1$ corresponds to a fully covered surface. The surface coverage decreases during the *on* time. For a typical discharge current of 10 A, the surface coverage reduces within 54 μs by half ($\theta = 0.5$) and to less than $\theta = 0.12$ within 200 μs. The surface coverage is a pronounced function of the discharge current (power) which is in line with calculations performed by Rezek *et al* [18] who concluded that the O/W flux ratio decreases with increasing discharge power. The surface coverage recovers during the *off* time. At the present conditions, it takes about 0.7 ms, 1.9 ms, and 2.7 ms for pulse length of 25 μs, 100 μs, and 400 μs, respectively, to reach a surface coverage $\theta = 90\%$. In all investigated cases, a full surface coverage with oxygen is reached again prior to the beginning of the following pulse. The inset of figure 10(a)

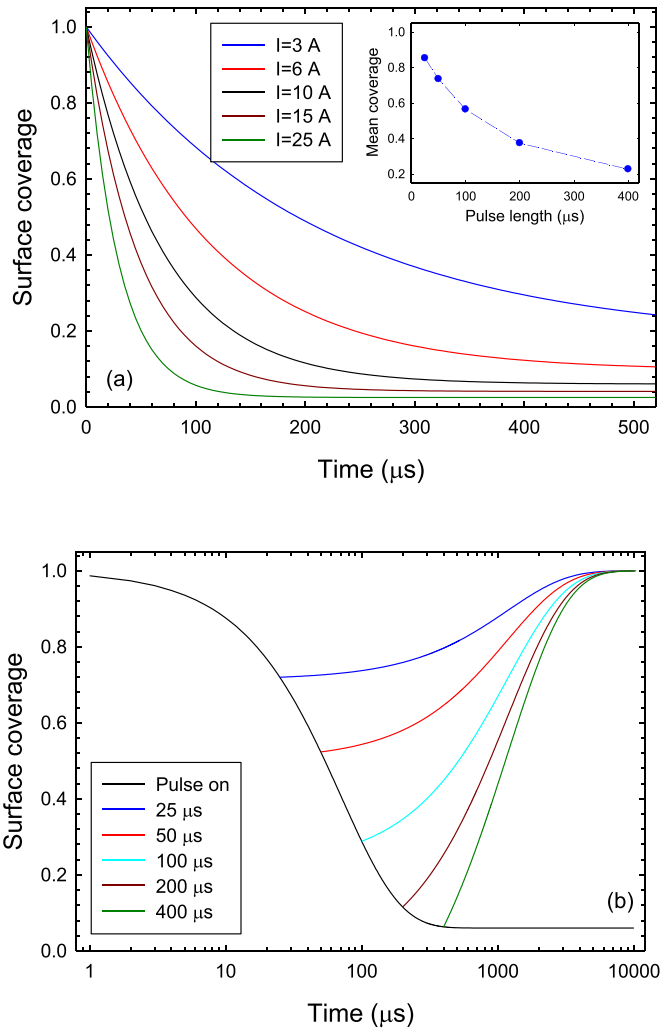

Figure 10. Temporal evolution of the relative surface coverage θ/θ_0 during the pulse. (a) For different discharge currents $I = 3$–25 A. Pulse length 500 μs, O_2 gas flow rate 10 sccm, partial O_2 gas pressure 0.5 Pa. (b) For different pulse lengths. Discharge current $I = 10$ A, O_2 gas flow rate 10 sccm, partial O_2 gas pressure 0.5 Pa. Effective cathode area 4.7 cm^2. Inset shows the time-averaged (mean) surface coverage during the pulse as function of pulse length and for a discharge current of 10 A.

shows the time-averaged surface coverage as function of pulse length. It amounts to 85%, 56%, and 23% for pulse length of 25 μs, 100 μs, and 400 μs, which is in quantitative agreement with results of Ganesan *et al* [22]. It confirms that the average surface oxygen coverage is larger during short pulses and smaller during long pulses which explains the decreasing fractions of O^+, WO^+, and WO_2^+ ions with increasing pulse length (figure 9).

According to the model, complete surface coverage with oxygen is achieved prior to a new pulse, regardless of the here employed pulse length. Therefore, the surface coverage alone does not explain the different initial behaviour of the pulse current as function of pulse length (figure 6). We know that the ion composition of the plasma changes during the pulse, as can be seen from the inset in figure 9. Positively charged ions are attracted by the negatively biased cathode

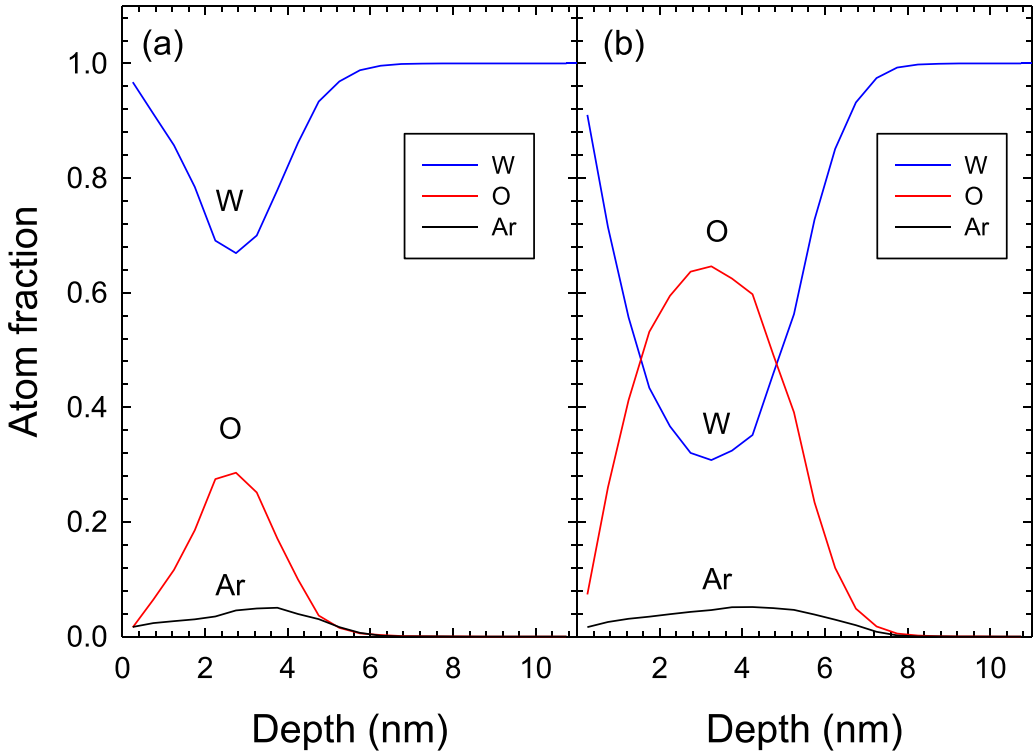

Figure 11. SDTrimSP simulation depth profiles at steady-state conditions (fluence 26.6 $\times 10^{20}$ ions m^{-2}) with (a) *low* O_2^+ fraction of 11.1% and (b) *high* O_2^+ fraction of 33.3%. Equal Ar^+ and W^+ ion fractions. Incident ion energy 970 eV.

and implanted into the surface which leads to the formation of an oxygen-containing sub-surface layer (SSL). The formation of such a SSL is studied with the help of SDTrimSp simulations (figure 11) which takes sputtering of target atoms and implantation by impinging ions into account. For simplicity, only impinging Ar^+, O_2^+, and W^+ ions with a kinetic energy of 970 eV are considered here. Two different simulations corresponding to *low* (≈20%) and *high* (≈50%) oxygen fractions of the bombarding plasma ions are carried out. The total fluence of impinging ions is 2.66×10^{21} m^{-2} to ensure steady-state conditions. According to the simulation, the SSL shows a broad spatial distribution of O atoms at a shallow mean depth of about 3 nm. The oxygen content of the SSL reaches up to 30% and more than 60% for the two cases with *low* and *high*, respectively, impinging oxygen fraction onto the surface. As expected, the oxygen composition of the SSL is strongly influenced by the oxygen fraction of the bombarding ions. The present results are in qualitative agreement with SSL formation results reported by Ganesan *et al* [22].

We know that the composition of the impinging ion flux depends on the pulse length, see figure 9. For example, the fraction of O^+, WO^+, and WO_2^+ ions is large during short pulses and a larger fraction of oxygen ions and atoms is implanted in comparison to long pulses. As a consequence, the fraction of implanted oxygen ions and atoms decreases with pulse duration and the oxygen composition of the SSL becomes smaller for long compared to short pulses. Calculations by Rezek *et al* also show a decrease of the target oxide fraction as function of pulse length [18]. However, the calculated decline is rather weak and quantitatively deviates from our observations.

The surface composition of two target surfaces, aluminium and tantalum, after reactive magnetron sputtering in argon with a 30% O_2 admixture was examined by Schelfhout *et al* [66]. Accordingly, the Al surface consists of Al_2O_3 and is therefore completely oxidised. In contrast, under otherwise similar conditions, the Ta target contains a significant amount of different suboxide states and even metallic tantalum is observed. The results also indicate that there are significant differences in the oxidation state for different target surfaces and that even with large oxygen admixtures of 50% or more, the target surface may not reach the fully oxidised Ta_2O_5 state. Similar conditions may prevail in the present case of a W target, which is chemically similar to Ta.

6. Conclusions

The pulse length dependence of a HiPIMS discharge with a W cathode was investigated. Discharge current, time-resolved optical emission spectra, and energy-resolved mass spectrometry results show pronounced dependencies on pulse length. In particular, the peak discharge current is larger for short (25 μs) and smaller for long (up to 500 μs) pulses. Energy-resolved mass spectrometry reveals that the fraction of oxygen and oxygen-containing ions like $WO_x^+ (x = 1, 2)$ decreases during long pulses. Time-resolved OES indicates a decreasing density of excited Ar and O atoms while the W

density increases during long pulses. There are at least three mechanisms to explain this behaviour. Firstly, gas depletion during the pulse reduces the Ar and O_2 density in front of the cathode. Secondly, the cathode is covered by oxygen atoms which desorb during the pulse *on* phase. Our simulations show that the resulting mean surface coverage with oxygen is larger for short compared to long pulses. Lastly, energetic oxygen and oxygen-containing ions impinging onto the cathode are implanted into the surface forming a sub-surface compound layer of implanted oxygen atoms which was investigated by SDTrimSp simulations. Our simulation results show that the cathode' surface coverage with oxygen changes during the pulse and that less oxygen is bound to the cathode for longer pulse length. The same holds for the oxygen content of the forming sub-surface layer which, due to the smaller oxygen fraction of impinging ions, also contains less oxygen for longer pulses. The changing oxygen surface coverage as well as the changing oxygen content of the sub-surface layer modifies the electronic properties of the surface and are thus responsible for different secondary electron emission yields as a function of time or pulse length. It explains the enhanced discharge current and the larger oxygen and oxygen-containing (WO_x^+) ion fraction during short pulses. The changing ion ratio should have a significant impact on film properties deposited during reactive HiPIMS. More detailed investigations are yet necessary to understand the pulse length dependence in more detail.

Data availability statement

The data that support the findings of this study are included within the article. Numerical data are available upon reasonable request from the corresponding author.

Acknowledgments

The work was partly supported by Project No. 21-04477S of the Czech Science Foundation and Project No. SOLID21-CZ.02.1.01/0.0/0.0/16_019/0000760 of the Operational Programme Research, Development and Education financed by European Structural and Investment Funds and the Czech Ministry of Education, Youth and Sports.

Conflict of interest

The authors declare that they have no known competing financial interests or personal relationships that could have appeared to influence the work reported in this paper.

Author contribution statement

All authors contributed equally to the work.

ORCID iDs

R Hippler https://orcid.org/0000-0002-5956-3321
M Cada https://orcid.org/0000-0001-6826-983X
A Mutzke https://orcid.org/0000-0003-0517-6817
Z Hubicka https://orcid.org/0000-0002-4051-057X

References

[1] Ellmer K 2008 *Low Temperature Plasmas* ed R Hippler, H Kersten, M Schmidt and K H Schoenbach (Weinheim: Wiley) p 675
[2] Gudmundsson J T 2020 Physics and technology of magnetron sputtering discharges *Plasma Sources Sci. Technol.* **29** 113001
[3] Strijckmans K and Depla D 2014 A time-dependent model for reactive sputter deposition *J. Phys. D: Appl. Phys.* **47** 235302
[4] Depla D, Mahieu S and De Gryse R 2009 Magnetron sputter deposition: linking discharge voltage with target properties *Thin Solid Films* **517** 2825
[5] Kouznetsov V, Macak K, Schneider J M, Helmersson U and Petrov I 1999 *Surf. Coat. Technol.* **122** 290
[6] Anders A 2011 *Surf. Coat. Technol.* **205** S1
[7] Stranak V *et al* 2009 *J. Phys. D: Appl. Phys.* **42** 105204
[8] Hrubantova A, Hippler R, Wulff H, Cada M, Olejnicek J, Nepomniashchaia N, Helm C A and Hubicka Z 2022 Deposition of tungsten oxide films by reactive magnetron sputtering on different substrates *J. Vac. Sci. Technol.* A **40** 063402
[9] Alami J, Sarakinos K, Uslu F, Klever C, Dukwen J and Wuttig M 2009 On the phase formation of titanium oxide films grown by reactive high power pulsed magnetron sputtering *J. Phys. D: Appl. Phys.* **42** 115204
[10] Stranak V, Cada M, Hubicka Z, Tichy M and Hippler R 2010 *J. Phys. D: Appl. Phys.* **108** 043305
[11] Anders A 2017 *J. Appl. Phys.* **121** 171101
[12] Wang C and Gomer R 1979 Sticking coefficients of CO, O_2 and Xe on the (110) and (100) planes of tungsten *Surf. Sci.* **84** 329
[13] Keraudy J, Delfour-Peyrethon B, Ferrec A, Garcia Molleja J, Richard-Plouet M, Payen C, Hamon J, Corraze B, Goullet A and Jouan P-Y 2017 Process- and optoelectronic-control of NiO_x thin films deposited by reactive high power impulse magnetron sputtering *J. Appl. Phys.* **121** 171916
[14] Hippler R, Cada M and Hubicka Z 2021 Direct current and high power impulse magnetron sputtering discharges with a positively biased anode *J. Vac. Sci. Technol.* A **39** 043007
[15] Hippler R, Cada M and Hubicka Z 2020 Time-resolved Langmuir probe diagnostics of a bipolar high power impulse magnetron sputtering discharge *Appl. Phys. Lett.* **116** 064101
[16] Rudolph M, Brenning N, Raadu M A, Hajihoseini H, Gudmundsson J T, Anders A and Lundin D 2020 Optimizing the deposition rate and ionized flux fraction by tuning the pulse length in high power impulse magnetron sputtering *Plasma Sources Sci. Technol.* **29** 05LT01
[17] Kozak T and Vlcek J 2016 A parametric model for reactive high-power impulse magnetron sputtering of films *J. Phys. D: Appl. Phys.* **49** 055202
[18] Rezek J, Kozak T, Kumar N and Haviar S 2021 Synergy of experiment and model for reactive HiPIMS: effect of discharge parameters on WO_x composition and deposition rate *J. Phys. D: Appl. Phys.* **54** 125202
[19] Yang Y-C, Chang C-T, Hsiao Y-C, Lee J-W and Lou B-S 2014 Influence of high power impulse magnetron sputtering pulse parameters on the properties of aluminum nitride coatings *Surf. Coat. Technol.* **259** 219–31
[20] Shimizu T, Zanaska M, Villoan R P, Brenning N, Helmersson U and Lundin D 2021 Experimental

verification of deposition rate increase, with maintained high ionized flux fraction, by shortening the HiPIMS pulse *Plasma Sources Sci. Technol.* **30** 045006
[21] Brenning N, Butler A, Hajihoseini H, Rudolph M, Raadu M A, Gudmundsson J T, Minea T and Lundin D 2020 Optimization of HiPIMS discharges: the selection of pulse power, pulse length, gas pressure and magnetic field strength *J. Vac. Sci. Technol.* A **38** 033008
[22] Ganesan R, Murdoch B J, Treverrow B, Ross A E, Falconer I S, Kondyurin A, McCulloch D G, Partridge J G, McKenzie D R and Bilek M M M 2015 The role of pulse length in target poisoning during reactive HiPIMS: application to amorphous HfO_2 *Plasma Sources Sci. Technol.* **24** 035015
[23] Ganesan R, Akhavan B, Partridge J G, McCulloch D G, McKenzie D R and Bilek M M M 2017 Evolution of target condition in reactive HiPIMS as a function of duty cycle: an opportunity for refractive index grading *J. Appl. Phys.* **121** 171909
[24] Viloan R P B, Zanaska M, Lundin D and Helmersson U 2021 Pulse length selection for optimizing the accelerated ion flux fraction of a bipolar HiPIMS discharge *Plasma Sources Sci. Technol.* **29** 125013
[25] Hnilica J, Klein P, Vasina P, Snyders R and Britun N 2020 Revisiting particle dynamics in HiPIMS discharges. II. Plasma pulse effects *J. Appl. Phys.* **128** 043304
[26] Meskinis Š, Vasiliauskas A, Andrulevicius M, Jurkeviciute A, Peckus D and Tamulevicius S 2019 Diamond like carbon films with embedded Cu nanoclusters deposited by reactive high power impulse magnetron sputtering: pulse length effects *Thin Solid Films* **673** 1
[27] Wang L, Jin J, Zhu C, Li G, Kuang X and Huang K 2019 Effects of HiPIMS pulse-length on plasma discharge and on the properties of WC-DLC coatings *Appl. Surf. Sci.* **487** 526
[28] Kumar N, Haviar S, Rezek J, Baroch P and Zeman P 2020 Tuning stoichiometry and structure of Pd-$WO_3 - x$ thin films for hydrogen gas sensing by high-power impulse magnetron sputtering *Materials* **13** 5101
[29] Magnus F, Tryggvason T K, Olafsson S and Gudmundsson J T 2012 Current–voltage–time characteristics of the reactive Ar/O_2 high power impulse magnetron sputtering discharge *J. Vac. Sci. Technol.* A **30** 050601
[30] Sushkov V, Do H T, Cada M, Hubicka Z and Hippler R 2013 Time-resolved tunable diode laser absorption spectroscopy of excited argon and ground-state titanium atoms in pulsed magnetron discharges *Plasma Sources Sci. Technol.* **22** 015002
[31] Hippler R, Cada M, Stranak V, Hubicka Z and Helm C A 2017 *J. Phys. D: Appl. Phys.* **50** 445205
[32] Hippler R, Cada M, Stranak V, Helm C A and Hubicka Z 2019 Pressure dependence of singly and doubly charged ion formation in a HiPIMS discharge *J. Appl. Phys.* **125** 013301
[33] Stranak V, Hubicka Z, Adámek P A J, Blažek J, Tichý M, Špatenka P, Hippler R and Wrehde S 2006 *Surf. Coat. Technol.* **201** 2512
[34] Stranak V, Quaas M, Wulff H, Hubicka Z, Wrehde S, Tichy M and Hippler R 2008 *J. Phys. D: Appl. Phys.* **41** 055202
[35] Cada M, Adamek P, Stranak V, Kment Š, Olejnicek J, Hubicka Z and Hippler R 2013 *Thin Solid Films* **549** 177
[36] Hippler R, Hubicka Z, Cada M, Ksirova P, Wulff H, Helm C A and Stranak V 2017 *J. Appl. Phys.* **121** 171906
[37] Hala M, Vernhes R, Zabeida O, Klemberg-Sapieha J-E and Martinu L 2014 Reactive HiPIMS deposition of SiO_2/Ta_2O_5 optical interference filters *J. Appl. Phys.* **116** 213302
[38] Hippler R, Cada M, Stranak V and Hubicka Z 2019 Time-resolved optical emission spectroscopy of a unipolar and a bipolar pulsed magnetron sputtering discharge in an argon/oxygen gas mixture with a cobalt target *Plasma Sources Sci. Technol.* **28** 115020
[39] Rosman K J R and Taylor P D P 1998 Isotopic compositions of the elements 1997 (Technical Report) *Pure Appl. Chem.* **70** 217
[40] Mutzke A, Schneider R, Eckstein W, Dohmen R, Schmid K, von Toussaint U and Badelow G 2019 SDTrimSP version 6.00 *IPP-Report* 2019-02 (Garching: Max-Planck-Institut für Plasmaphysik)
[41] Eckstein W 1991 *Computer Simulation of Ion-Solid Interactions* (*Springer Series in Material Science*) vol 10 (Berlin: Springer)
[42] Mutzke A, Bandelow G and Schneider R 2015 Sputtering of mixed materials of beryllium and tungsten by hydrogen and helium *J. Nucl. Mater.* **467** 413
[43] Hofsäss H, Zhang K and Mutzke A 2014 Simulation of ion beam sputtering with SDTrimSP TRIDYN and SRIM *Appl. Surf. Sci.* **310** 134
[44] Anders A, Capek J, Hala M and Martinu L 2012 The 'recycling trap': a generalized explanation of discharge runaway in high power impulse magnetron sputtering *J. Phys. D: Appl. Phys.* **45** 012003
[45] Brenning N, Gudmundsson J T, Raadu M A, Petty T J, Minea T and Lundin D 2017 *Plasma Sources Sci. Technol.* **26** 125003
[46] Aiempanakit M, Aijaz A, Lundin D, Helmersson U and Kubart T 2013 Understanding the discharge current behavior in reactive high power impulse magnetron sputtering of oxides *J. Appl. Phys.* **113** 133302
[47] Layes V, Corbella C, Thiemann-Monjé S, Schulz-von der Gathen V, von Keudell A and de los Arcos T 2018 Connection between target poisoning and current waveforms in reactive high-power impulse magnetron sputtering of chromium *Plasma Sources Sci. Technol.* **27** 084004
[48] Gudmundsson J T, Lundin D, Brenning N, Raadu M A, Huo C and Minea T M 2016 *Plasma Sources Sci. Technol.* **25** 065004
[49] Kubart T and Aijaz A 2017 Evolution of sputtering target surface composition in reactive high power impulse magnetron sputtering *J. Appl. Phys.* **121** 171903
[50] Kubart T, Gudmundsson J T and Lundin D 2020 Reactive high power impulse magnetron sputtering *High Power Impulse Magnetron Sputtering* ed D Lundin, T Minea and J T Gudmundsson (Amsterdam: Elsevier) ch 6, p 223
[51] Bernatova K, Klein P, Hnilica J and Vasina P 2021 Temporal studies of titanium ionised density fraction in reactive HiPIMS with nitrogen admixture *Plasma Sources Sci. Technol.* **30** 125002
[52] Shimizu T, Takahashi K, Boyd R, Viloan R P, Keraudy J, Lundin D, Yang M and Helmersson U 2021 Low temperature growth of stress-free single phase α-W films using HiPIMS with synchronized pulsed substrate bias *J. Appl. Phys.* **129** 155305
[53] Pajdarova A D, Vlcek J, Kudlacek P and Lukas J 2009 Electron energy distributions and plasma parameters in high-power pulsed magnetron sputtering discharges *Plasma Sources Sci. Technol.* **18** 025008
[54] Poolcharuansin P and Bradley J W 2010 *Plasma Sources Sci. Technol.* **19** 025010
[55] Thompson M W 1968 *Phil. Mag.* A **18** 377
[56] Betz G and Husinsky W 2004 *Phil. Trans. R. Soc.* A **362** 177
[57] Angelin E J and Hippler R 2017 *Nucl. Instrum. Methods Phys. Res.* B **407** 132
[58] Schelfhout R, Strijckmans K and Depla D 2020 Sputter yield measurements to evaluate the target state during reactive magnetron sputtering *Surf. Coat. Technol.* **399** 126097

[59] Taglauer E, Heiland W and Onsgaard J 1980 Ion beam desorption of surface layers *Nucl. Instrum. Methods* **168** 571
[60] Ghose D, Brinkmann U and Hippler R 1995 Light emission from a Si target during ion beam sputtering *Surf. Sci.* **327** 53
[61] Li J, Hoekstra B, Wang Z-B, Qiu J and Pu Y-K 2018 Secondary electron emission influenced by oxidation on the aluminum surface: the roles of the chemisorbed oxygen and the oxide layer *Plasma Sources Sci. Technol.* **27** 044002
[62] Greiner M T, Chai L, Helander M G, Tang W-M and Lu Z-H 2012 Transition metal oxide work functions: the influence of cation oxidation state and oxygen vacancies *Adv. Funct. Mater.* **22** 4557
[63] Yamamura Y and Shindo S 1984 An empirical formula for angular dependence of sputtering yields *Radiat. Eff.* **80** 57
[64] Oechsner H 1973 Untersuchungen zur Festkörperzerstäubung bei schiefwinkligem Ionenbeschuß polykristalliner Metalloberflächen im Energiebereich um 1 keV *Z. Phys.* A **261** 37
[65] Taglauer E, Beitat U, Marin G and Heiland W 1976 Sputtering of adsorbed layers by ion bombardment *J. Nucl. Mater.* **63** 193
[66] Schelfhout R, Strijckmans K and Depla D 2018 An x-ray photoelectron spectroscopy study of the target surface composition after reactive magnetron sputtering *Surf. Coat. Technol.* **353** 231